Universiteit Leiden
The Netherlands

Accelerating the photocatalytic water splitting in catalyst-dye complexes

Shao, Y.

Citation
Shao, Y. (2021, February 24). *Accelerating the photocatalytic water splitting in catalyst-dye complexes*. Retrieved from https://hdl.handle.net/1887/3147173

Version:	Publisher's Version
License:	Licence agreement concerning inclusion of doctoral thesis in the Institutional Repository of the University of Leiden
Downloaded from:	https://hdl.handle.net/1887/3147173

Note: To cite this publication please use the final published version (if applicable).

Cover Page

Universiteit Leiden

The handle http://hdl.handle.net/1887/3147173 holds various files of this Leiden University dissertation.

Author: Shao, Y.
Title: Accelerating the photocatalytic water splitting in catalyst-dye complexes
Issue date: 2021-02-24

CHAPTER 5

Two-Channel Model for Electron Transfer in a Dye–Catalyst–Dye Supramolecular Complex

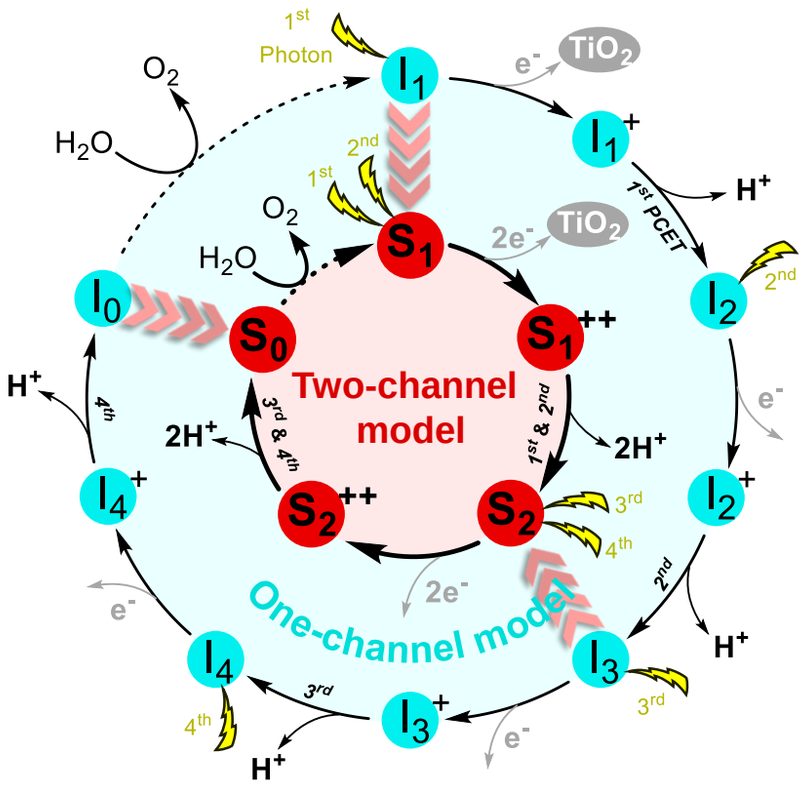

This chapter is to be submitted as:

Two-Channel model for Electron Transfer in a Dye–Catalyst–Dye Supramolecular Complex for Photocatalytic Water Splitting, **2021**, to be submitted.

5

Abstract

To improve the performance of DS-PEC devices for splitting water, the tailoring of the photocatalytic four-photon water oxidation half-reaction represents a principle challenge of fundamental significance. Here we consider a Ru-based WOC covalently bound to two NDI dye functionalities providing comparable driving forces and channels for electron transfer. Constrained AIMD simulations are performed to investigate the photocatalytic cycle of this two-channel model for photocatalytic water splitting. The introduction of a second light-harvesting dye in the Ru-based dye–WOC–dye supramolecular complex enables two separate electron-transfer channels, leading to a five-step catalytic cycle with three intermediates and two doubly oxidized states. The total spin S = 1 is conserved during the catalytic process, and the system proceeds from the Ru=O intermediate to the final Ru–O_2 intermediate with a triplet molecular O_2 ligand that is eventually released into the environment. The in-depth insight into the proposed photocatalytic cycle of the two-channel model provides a strategy for the development of novel high-efficiency supramolecular complexes for DS-PEC devices with conservation of spin multiplicity along the reaction coordinate as a guiding principle.

5.1. Introduction

Artificial photosynthesis, inspired by nature, with the goal of conversion of solar energy into chemical energy, has attracted growing interest in the past decades.[1-2] In particular, DS-PECs that can drive water splitting through the absorption of sunlight, have the potential to produce clean and renewable chemical fuels, *e.g.* in the form of molecular energy-rich hydrogen, to meet the future global energy demand in an environmentally sustainable way.[3-7] Two half reactions are involved when the water splitting process proceeds in two physically separated electrode compartments, the oxygen evolution reaction (OER) for water oxidation, and the hydrogen evolution reaction (HER) for proton reduction.[8-9] For the catalytic water splitting in DS-PECs, the high activation free energy barrier for the O–O bond formation process represents a thermodynamic and kinetic bottleneck, and the OER half-reaction is considered the rate-determining step.[10-11]

The solar-driven four-photon water oxidation half-reaction occurs at the photoanode, and is always initiated by light absorption at the molecular sensitizers and subsequent electron injection from the dye in the excited state into the electrode. Owing to a proper molecular assembly of the WOC and the dye components in a WOC–dye supramolecular complex, the photooxidation of the dye should be followed by a PCET[12-16] process within the water oxidation catalytic cycle: The electron is used for the regeneration of the dye to its initial state, while the proton is being transferred to a different direction, into the environment.[17] Computational studies serve as a powerful technique for guiding the development of efficient dye-sensitized photoanodes[18-23] by rate enhancement of photocatalytic water oxidation in DS-PEC devices and the modulation of the mechanism of operation by the solvent environment[24-26]. A great majority of the computational effort has been devoted to lowering the activation free energy barrier of the third catalytic water oxidation step involving the rate-limiting O–O bond formation process, in which a single channel for the ET from the WOC to the photooxidized dye was explored.[26]

Since 1970, Kok's classical *S*-state cycle model of photosynthetic water oxidation involving five oxidation states ($S_{0\rightarrow4}$) has been the paradigm for the understanding of oxygen evolution.[27] By taking into account the role and sequence of deprotonation events as well, an extended *S*-state cycle has been

introduced by Dau *et al.*, in which eight successive steps starting from I_0 lead to I_8 and only then the O_2 is formed and released.[28] In other words, the *I*-cycle model involves not only four oxidizing equivalents but also four bases prior to the dioxygen formation. For sequential alternating proton and electron transfer[17] or concerted PCET[26] according to the Kok or Dau cycle in natural or artificial oxygenic photosynthesis, every individual catalytic PCET step can only proceed after the accomplishment of the previous catalytic step.[29] We conjecture that the overall efficiency of oxygenic photosynthesis would be reasonably improved if catalytic steps could run from two excited dye motifs in parallel, and thereby combining two PCET steps without stable intermediates in between.

Scheme 5.1. Proposed photocatalytic cycle of the two-channel model for water splitting by a Ru-based dye–WOC–dye system[a]

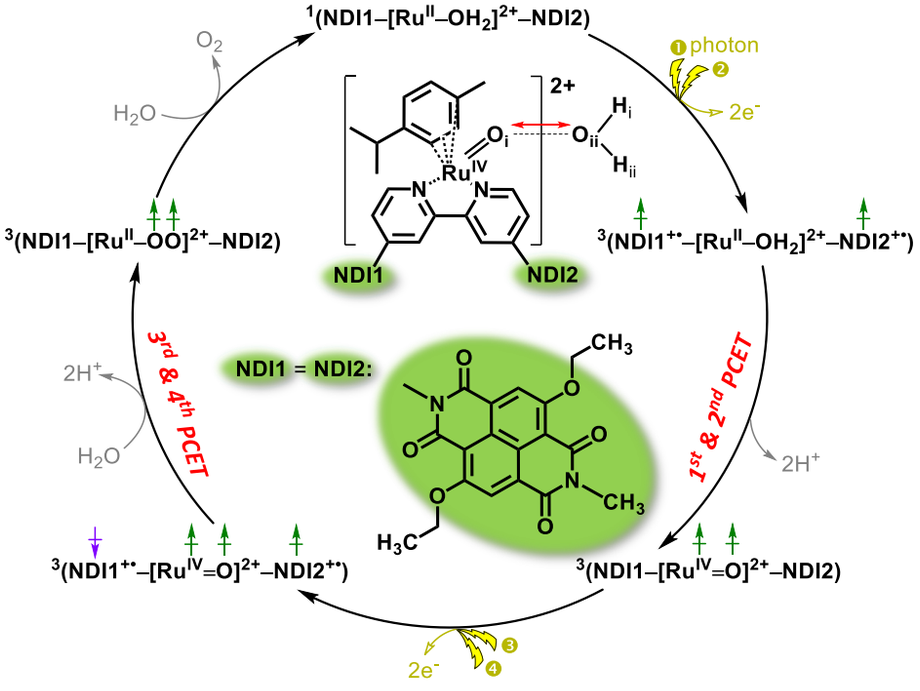

[a]Schematic Structure of the third intermediate ^{3}(NDI1–[(cy)Ru^{IV}(O)bpy]$^{2+}$–NDI2) complex (indicated as ^{3}(NDI1–[Ru^{IV}=O]$^{2+}$–NDI2)) together with the attacking water molecule, as explicitly shown in the inset. It is assumed that each light flash induces an electron injection (golden arrows) from the NDI1/NDI2 to the semiconductor electrode or to the next stage in a tandem cell, leading to the photooxidation of NDI1/NDI2: NDI1/NDI2 → NDI1$^{+\bullet}$/NDI2$^{+\bullet}$. Green (α electrons) and purple (β electrons) vertical arrows depict the spin of unpaired electrons located on the WOC and on the two NDI dyes. The red double-sided arrow indicates the reaction coordinate d(O$_i$←O$_{ii}$) considered in the constrained MD simulations. The superscript on the left indicates the spin multiplicity 2S+1 for each intermediate and oxidized state.

In this work an additional dye molecule is introduced in the catalyst–dye supramolecular complex ^{1}([(cy)Ru^{II}bpy(H$_2$O)]$^{2+}$–NDI) (cy = *p*-cymene, bpy = 2,2′-bipyridine, NDI = 2,6-diethoxy-1,4,5,8-diimide-naphthalene) for photocatalytic water splitting, which has been systematically investigated *in silico* recently,[17, 26, 30] leading to the dye–WOC–dye supramolecular complex ^{1}(NDI1–[(cy)Ru^{II}bpy(H$_2$O)]$^{2+}$–NDI2) with the total spin S = 0 (indicated shortly as ^{1}(NDI1–[Ru^{II}–H$_2$O]$^{2+}$–NDI2) in Scheme 5.1, where NDI1 = NDI2 = NDI). The goal of this modification is to rearrange the sequence of catalytic intermediates by having first the absorption of two photons, followed by the transfer of two electrons and two protons. The incorporation of two NDI dye functionalities covalently bound to the bipyridine ligand of the catalytic motif, provides two parallel channels for ET, enabling theoretically concurrent ET events from the WOC to the oxidized dyes NDI1$^{+\bullet}$ and NDI2$^{+\bullet}$. Scheme 5.1 presents the proposed photocatalytic cycle of the two-channel model for water splitting by the Ru-based dye–WOC–dye system. An extended photocatalytic cycle considering all possible reaction pathways is reported in Scheme A5.1 for completeness (See Appendix 5.A.2). Given that the spin alignment of unpaired electrons on the WOC and dye has turned out to play a significant role in the PCET reactions in the one-channel model (see **Chapter 2** of this thesis), only the most favorable pathways with proper spin alignments are explored for the two-channel model (see Scheme 5.1). Specifically, the first half of the cycle for the two-channel model is initiated by the co-photooxidation of two NDI dyes, which leaves one α unpaired electron (↟) on each NDI dye with the total spin S = 1. This choice is based on the previous finding for the one-channel model where the triplet spin configuration was found to be more favorable for the second PCET step. Instead, for the third step involving the O–O bond formation process in the one-channel model, it is found that the antiparallel spin alignment of the unpaired electrons on the WOC (↟ ↟) and dye (↡) is essential for this reaction. Thus for the second half of the cycle, the antiparallel spin alignment of unpaired electrons on the two NDI dyes is considered: in this way the total spin S = 1 is preserved until the formation of the triplet oxygen, which eventually leaves the complex and brings the spin multiplicity back to the singlet state (see Scheme 5.1).[17]

Here, we report how the introduction of parallel channels for ET changes the number of involved intermediates and the sequence of reaction events along the

photocatalytic cycle in the dye–WOC–dye system by using AIMD simulations, which can provide accurate predictions of the reaction mechanism and activation energy barrier.[31] Since the catalytic step involving the O–O bond formation has long been considered the rate-limiting step for the photocatalytic water oxidation half-reaction, we focus on the second half of the catalytic cycle starting from the second intermediate ^{3}(NDI1–[Ru^{IV}=O]$^{2+}$–NDI2) (see bottom right in Scheme 5.1) to provide insight into the impact of the two electron-transfer channels on the reaction efficiency.

5.2. Results and Discussion

5.2.1 Geometry Optimization of the Dye–WOC–Dye Complex with DFT.

The initial geometry of the dye–WOC–dye complex ^{3}(NDI1–[Ru^{IV}=O]$^{2+}$–NDI2) was optimized at the DFT level employing the OPBE exchange-correlation functional[32] and the TZP (triple-ζ polarized) Slater-type basis set with the ADF software package[33-34] (see Appendix 5.A.1 for more computational details).[30] To check if the photooxidized dyes coupled to the Ru-based WOC exert thermodynamic driving forces for the subsequent catalytic steps, the frontier molecular orbital energy levels together with the singly occupied molecular orbitals (SOMOs) of the doubly-oxidized complex ^{3}(NDI1$^{+\bullet}$–[Ru^{IV}=O]$^{2+}$–NDI2$^{+\bullet}$) with total spin S = 1 (see Scheme 5.1) are shown in Figure A5.1 and the corresponding energy values are listed in Table A5.1 (see Appendix 5.A.3). A closed systems approach simulation[35] with S = 1 allows to have the same total spin for the initial (^{3}[Ru^{IV}=O]$^{2+}$) and for the final (^{3}[Ru^{II}–O$_2$]$^{2+}$) intermediates, thus avoiding the need for intersystem crossing during the reaction: The electronic state of the ^{3}[Ru^{IV}=O]$^{2+}$ WOC is in a triplet configuration, while the two unpaired electrons on the photooxidized dyes are in an antiparallel arrangement. It is found that both the alignment of the energy levels and the spin alignment are favorable for the subsequent ET steps involving the O–O bond formation since the SOMOs localized on the NDI dyes (SOMO dye1 and SOMO dye2) with antiparallel spins are lower in energy than the HOMO of the dye–WOC–dye complex localized on the WOC (SOMO WOC) (see Figure A5.1). The orbital energy difference between the SOMO WOC and the SOMO dyes is $\Delta E_{SOMO\text{-}1}$ = ~0.18 and $\Delta E_{SOMO\text{-}2}$ = ~0.21 eV, respectively (see Table A5.1).

5.2.2 Equilibration of the System and Photooxidation of two NDI Dyes.

An orthorhombic box of dimensions 25.5 × 22.4 × 15.4 Å^3 with periodic boundary conditions containing the dye–WOC–dye solute ^{3}(NDI1–[Ru^{IV}=O]$^{2+}$–NDI2) (S = 1) together with 212 explicit water molecules was used in the AIMD simulations to get accurate predictions of the catalytic reaction and free energy profile. AIMD simulations were carried out with the CPMD program.[36] The electronic structure was determined using GTH pseudopotentials for the ruthenium transition metal[37] and dispersion-corrected pseudopotentials (DCACP) for the remaining atoms[38], together with a plane wave cutoff of 70 Ry and the OPBE exchange–correlation functional[32] (see Appendix 5.A.1 for more computational details). An initial free AIMD simulation of 0.6 ps at room temperature (300 K) was performed for the solvated system to further equilibrate the solvation environment (see section 5.A.1.2).

The system is assumed to be already in its doubly-oxidized form of dye$^{+\bullet}$–[WOC]$^{2+}$–dye$^{+\bullet}$ at the beginning of the constrained AIMD simulation for the second half of the cycle, since the photoinduced electron injection from the selected NDI to a TiO_2 semiconductor surface can be achieved on a time scale of ~1 ps, as has been demonstrated in previous work.[30] The photooxidation is mimicked by removing two electrons from the simulation box after the initial equilibration simulation of the dye–WOC–dye system leading to a total charge of 4+. A free AIMD simulation for another 0.6 ps at room temperature is performed to further equilibrate the fully oxidized system with the total spin S = 1 corresponding to antiparallel spins on the two NDI dyes. This antiparallel spin alignment refers to the most favorable reaction pathway for the one-channel model reported in our recent work, where the total spin angular momentum S = 1 was assumed to be conserved in the AIMD simulation studies, since the O–O bond formation was thermodynamically unfavorable for the parallel spin alignment on WOC and dye with S = 2.[17] When tracking the spin density along the free AIMD simulation, it is found that two unpaired α electrons (↟) localize on the WOC at the Ru^{IV}=O group, one unpaired β electron (↓) on NDI1, and one unpaired α electron (↟) on NDI2 in the system after the photooxidation of the two NDI dyes (see the inset in Figure A5.2). No ET occurs at this stage, which is an indication of the stability of the initial state of the oxidized complex ^{3}(NDI1$^{+\bullet}$–[Ru^{IV}=O]$^{2+}$–NDI2$^{+\bullet}$) (S = 1).

5.2.3 Constrained AIMD Simulations and Catalytic Water Oxidation Steps.

To explore the catalytic water oxidation steps involving bond-forming and bond-breaking processes, which are normally considered as rare events on the characteristic AIMD simulation time scale, the constrained MD approach was employed in the simulations to control the reaction coordinate after the re-equilibration of the photooxidized system.[39] The constrained reaction coordinate in this case is the distance between the oxygen atom O_i on the Ru complex and the O_{ii} oxygen of the attacking water indicated by the red double-sided arrow in

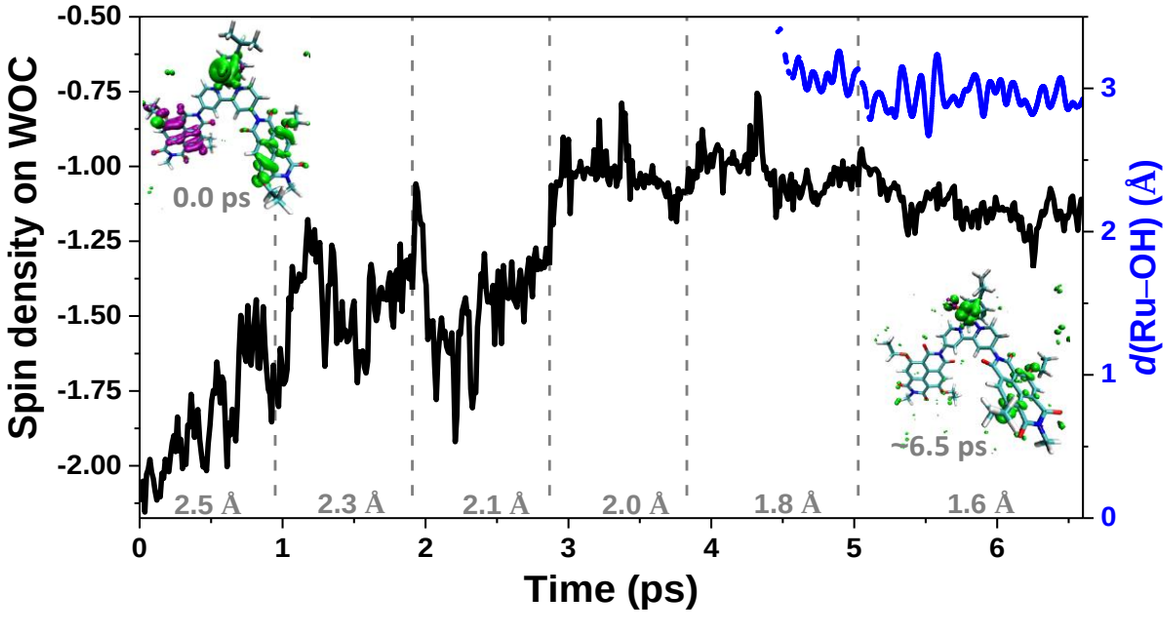

Figure 5.1. Spin density integrated over the upper half of the simulation box including the WOC (black line) and time evolution of the distance between Ru and the OH *d*(Ru–OH) (blue line) along the constrained MD trajectories. The OH is defined as an O atom with only one H within a radius of 1.2 Å, illustrating the PT during the MD simulations. Inset left shows the spin density isosurface computed at a snapshot taken at the beginning of the constrained 2.5 Å MD simulation (0.0 ps), clearly indicating two unpaired α electrons (↟ in green) localized on the catalyst, one unpaired β electron on NDI1 (↡ in purple), and one unpaired α electron on NDI2 (↟ in green). Inset right shows the spin density isosurface computed at the end of the constrained 1.6 Å simulation (~6.5 ps). According to the simulations, one proton of the attacking water is totally released during the constrained 1.6 Å simulation and only oxygen O_{ii} is in the OH form at any time. An integrated spin density value of –2 corresponds to two unpaired α electron (↟). The value of the constrained reaction coordinate $d(O_i \leftarrow O_{ii})$ in the MD simulations is noted in grey. The water molecules are omitted for clarity in both cases and only the initial intermediate $^3(NDI1^{+\bullet}–[Ru^{IV}=O]^{2+}–NDI2^{+\bullet})$ (S = 1) and the transient final intermediate $^3(NDI1–[Ru^{III}–OOH]^{2+}–NDI2^{+\bullet})$ (S = 1) are shown explicitly. See Scheme 5.1 for the atomic labelling.

Chapter 5

Scheme 5.1 (see Appendix 5.A.1 for more computational details). In order to visualize when and how the electron transfers from the WOC to the oxidized NDI dyes (see NDI1 and NDI2 in Scheme 5.1), the spin density was tracked during the AIMD simulations. The variation of the spin density localized on the WOC (black line) together with the time evolution of the distance between Ru and the OH d(Ru–OH) (blue line) along the constrained MD trajectories are collected in Figure 5.1. The initial value of –2 for the spin density corresponds to the triplet state with two unpaired electrons on the WOC.

For the two-channel model starting with the oxidized ^{3}(NDI1$^{+\bullet}$–[Ru^{IV}=O]$^{2+}$–NDI2$^{+\bullet}$) (S = 1) complex (see Figure 5.1, inset (left)), the ET starts at the reaction coordinate d(O_i←O_{ii}) = 2.5 Å (see Figure 5.1, black line), while in the one-channel model it was actually observed at the reaction coordinate d(O_i←O_{ii}) = 2.1 Å.[17] The shortening of d(O_i←O_{ii}) from 2.5 Å to 2.0 Å induces the complete ET from the WOC to the oxidized NDI1 with spin density localized on the WOC fluctuating around an average value of –1. After short-term fluctuations of spin density localized on the WOC, the dye system that is initially in the dye$^{+\bullet}$–[WOC]$^{2+}$–dye$^{+\bullet}$ state ends up with one unpaired α electron (↟) localized on the WOC and one unpaired α electron (↟) on the NDI2 at the end of the constrained 1.8 Å MD simulation. Moreover, the PT from the attacking water molecule to the solvent is first observed during the constrained 1.8 Å MD simulation when tracking the distance between Ru and the OH d(Ru–OH) along the constrained MD trajectories (see Figure 5.1, blue line): here the OH is defined as an O atom with only one H within a radius of 1.2 Å. Subsequently, the released proton H_i diffuses into the solvent bulk via a "chain" of hydrogen-bonded water molecules following a Grotthuss-type mechanism[17, 23, 30, 40-41] and no back reaction occurs after ~5.2 ps along the constrained 1.6 Å MD trajectory (see Appendix 5.A.5). It is also noticeable that during the constrained 1.6 Å MD simulation, the integrated spin density gets an average value smaller than –1, which can be attributed to the initial attempts of the fourth ET process from the WOC to the oxidized NDI2 (see Figure 5.1, inset (right)).

At the end of the constrained 1.6 Å MD simulation, the constraint on the reaction coordinate was released and the system is allowed to evolve freely. The time evolution of the distance between the oxygen atoms O_i and O_{ii} d(O_i–O_{ii}), the variation of the total spin density localized on the WOC, and the distance

between Ru and H_3O^+ (defined as an O atom with three H within a radius of 1.2 Å) along the free MD trajectory after releasing the constraint are collected in Figure 5.2 for quantitative descriptions of electron and proton dynamics.

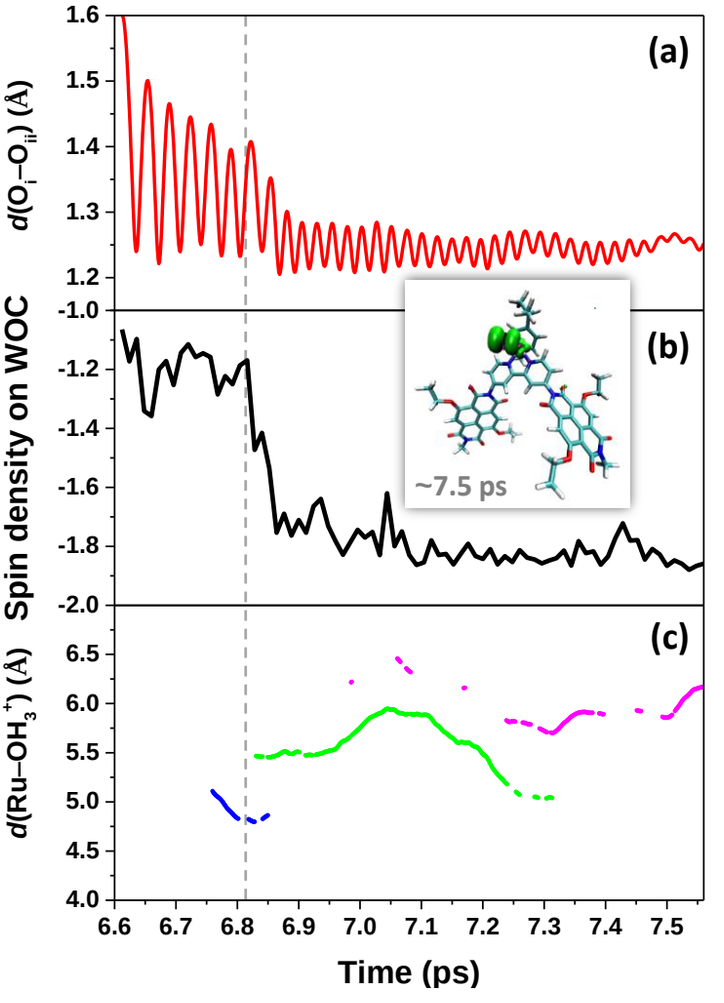

Figure 5.2. (a) Time evolution of the geometrical parameter $d(O_i–O_{ii})$, (b) spin density integrated over upper half of the simulation box including the WOC, and (c) distance between Ru and the H_3O^+ $d(Ru–OH_3^+)$ along the free MD trajectory after releasing the constraint at the end of the constrained 1.6 Å MD simulation. The H_3O^+ is defined as an O atom with 3 H within a radius of 1.2 Å, illustrating the second PT during the MD simulation. According to the simulations, only one oxygen is in the H_3O^+ form at any time, and the second excess proton associates primarily to three different oxygens (indicated with different colors: blue, green, and magenta) during the simulation. An integrated spin density value of –2 corresponds to two unpaired α electrons (‡). The inset shows the spin density isosurface computed for a snapshot taken at the end of the free MD simulation, which indicates clearly that the spin density is mostly localized on the O_2 ligand and shows the characteristic shape expected for the oxygen molecule. The water molecules are omitted for clarity and only the final intermediate NDI1–$[Ru^{II}–OO]^{2+}$–NDI2 (S = 1) is shown explicitly. The time range is consistent with Figure 5.1. See Scheme 5.1 for the atomic labelling.

Scheme 5.2. Four PCET steps between the catalytic intermediates from S_1^{2+} to S_0^{2+} for the supramolecular dye–WOC–dye complex[a]

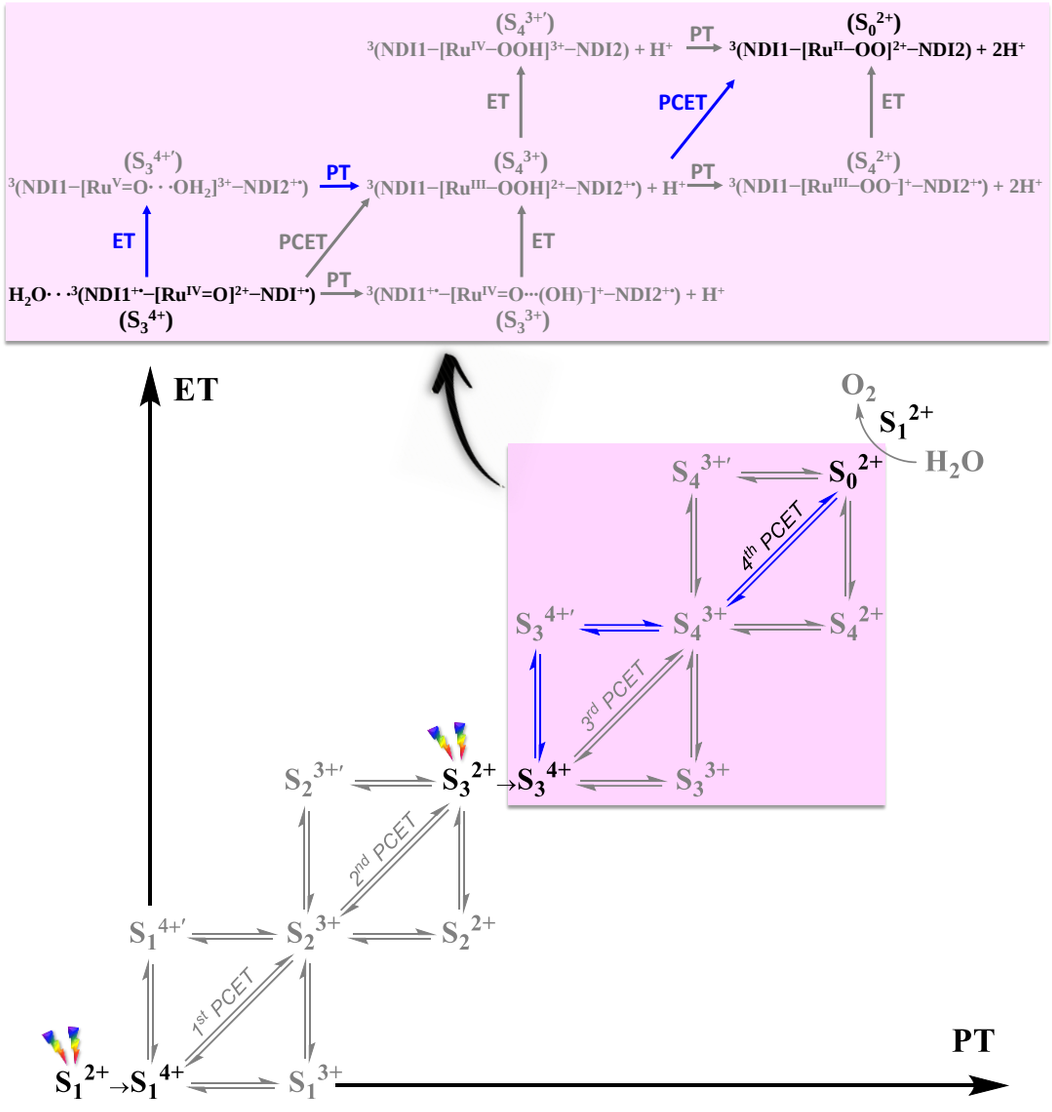

[a]It is assumed that two light flashes induce the cophotooxidation of the two NDI dyes in the two-channel model ($S_i^{2+} \rightarrow S_i^{4+}$, i = 0 – 4: NDI1 → NDI1$^{+\bullet}$ and NDI2 → NDI2$^{+\bullet}$). The vertical and horizontal double arrows correspond to the pathways of a sequential PCET mechanism, either ET from the WOC to the oxidized dye first ($S_i^{4+} \rightarrow S_i^{4+\prime}$ and $S_i^{3+} \rightarrow S_i^{3+\prime}$) or PT to the solvent first ($S_i^{4+} \rightarrow S_i^{3+}$ and $S_i^{3+} \rightarrow S_i^{2+}$). The diagonal double arrow denotes the concerted PCET mechanism. The favorable pathway of the second half of the catalytic cycle in the two-channel model is indicated in blue. The stable intermediates investigated in the present study are shown in black. The ligand exchange $S_0^{2+} + H_2O \rightarrow S_i^{2+} + O_2$ is also indicated in grey. H^+ represents the proton transferred to the solvent. The catalytic steps from S_3^{4+} to S_0^{2+}, which are the main focus of this work, are specifically described in the top panel.

Based on these data, the O–O bond distance relaxes within a very short time of ~0.2 ps to an average value of $d(O_i–O_{ii})$ = ~1.35 Å (see Figure 5.2a), which is

consistent with the formation of a transient Ru–OOH state in the third catalytic water oxidation step (for comparison, the O–O bond length in molecular hydrogen peroxide is 1.47 Å). After 0.2 ps (at ~6.8 ps in Figure 5.2, dashed vertical line) a fast ET process from the WOC to the oxidized NDI2 takes place (see Figure 5.2b). This ET process is strongly coupled to the fourth PT from the hydroperoxo ligand to the solvent bulk (see Figure 5.2c). Notice that two protons (H_i and H_{ii}) diffuse independently from each other into the solvent at this stage and we only focus on the second released proton H_{ii} in Figure 5.2c. The distance between the oxygen atoms O_i and O_{ii} equilibrates quickly to an average value $d(O_i–O_{ii})$ of ~1.25 Å. Although we have a higher proton density compared to the one-channel model, we observe that the fourth PCET catalytic water oxidation step proceeds spontaneously following the formation of the O–O bond. Subsequently the system reaches the final intermediate ^{3}(NDI1–[Ru^{II}–OO]$^{2+}$–NDI2) (S = 1) (see Scheme 5.1 and eq. 5.1, where H_2O_{sol} and H^+_{sol} represent the solvated attacking water molecule and solvated proton respectively).

$$^3(NDI1^{+\bullet}–[Ru^{IV}=O]^{2+}–NDI2^{+\bullet}) + H_2O_{sol} \quad \leftrightarrow \quad ^3(NDI1–[Ru^{II}–OO]^{2+}–NDI2) + 2H^+_{sol} \qquad (5.1)$$

In this final complex with an average value of $d(O_i–O_{ii})$ = ~1.25 Å two unpaired α electrons (↑) are localized on the dioxygen ligand (see Figure 5.2, inset), indicating the formation of the O=O double bond in the triplet state as in molecular oxygen (the O=O bond length in molecular O_2 in the triplet state is 1.21 Å for comparison). The O_2 ligand can then be exchanged by a water molecule and the complex is ready for the next catalytic cycle. All these results indicate that the third and fourth catalytic steps proceed in a concerted way with no stable intermediate between these two steps. This result is at variance with the case of the one-channel model since the complex with a hydroperoxo ligand is a stable intermediate in the one-channel model, while it is here only a transient Ru–OOH state developing into the final intermediate (see Scheme 5.2).[17]

5.2.4 Free Energy Profile and Reaction Rate Evaluation.

Having established that the second half of the catalytic water oxidation cycle starting from the doubly photooxidized supramolecular complex ^{3}(NDI1$^{+\bullet}$–[Ru^{IV}=O]$^{2+}$–NDI2$^{+\bullet}$) (S = 1) proceeds combining two sequential steps without stable intermediates in between, it is relevant to evaluate how difficult it

is to activate these reactions in such a two-channel model. The reaction coordinate $d(O_i \leftarrow O_{ii})$ is constrained to a series of fixed values to estimate the free energy profile along this reaction pathway using the Blue Moon ensemble approach and thermodynamic integration (see Appendix 5.A.1.3 for more details).[39, 42-43] The time-averaged mean forces associated with the applied constraints, the interpolation of the time-averaged mean forces used for this analysis, and the corresponding free energy profile of the two-channel model as a function of the reaction coordinate $d(O_i \leftarrow O_{ii})$ are reported in Figure 5.3 (see Appendix 5.A.1.3 for computational details). Table 5.1 summarizes the thermodynamics parameters for the O–O bond formation process extracted from these results.

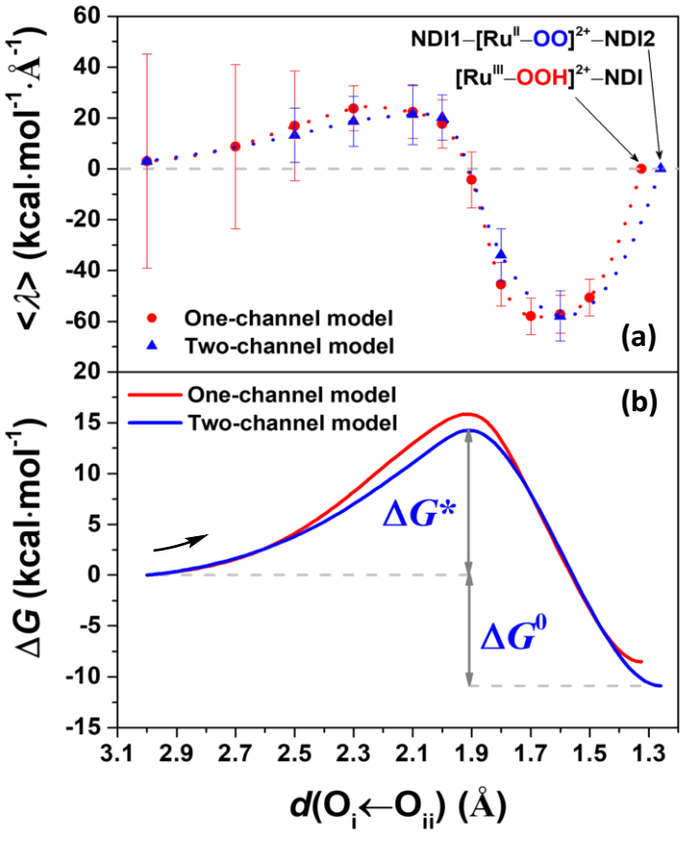

Figure 5.3. (a) Time-averaged constraint force represented by the Lagrangian multiplier $\langle\lambda\rangle$ computed for each constrained MD simulation as a function of the reaction coordinate $d(O_i \leftarrow O_{ii})$ in the two-channel model. The Akima splines (100 points) is used to interpolate the mean forces. The final intermediates corresponding to the MD simulations for the one-channel and two-channel models are both indicated. (b) Free energy profile along the reaction coordinate $d(O_i \leftarrow O_{ii})$ computed by thermodynamic integration. The time-averaged constraint forces and associated free energy profile obtained in the one-channel model from a previous study is also presented for comparison (see Ref. 17). The error bars indicate the standard deviations.

Table 5.1. The calculated activation energy barrier (ΔG^* in kcal mol^{-1}), reaction driving force (ΔG^o in kcal mol^{-1}), and the reaction rate (k in s^{-1}) corresponding to the one-/two-channel models. The results for the one-channel model are taken from ref. 17.

Model	ΔG^*	ΔG^o	k
One-channel[17]	15.9	–8.5	15.7
Two-channel	14.3	–10.9	230.4

The calculated activation free energy barrier (ΔG^*) for the two-channel model is 14.3 kcal mol^{-1} (~0.62 eV), which is slightly lower than the 15.9 kcal mol^{-1} (~0.69 eV) computed with the same approach for the one-channel model[17] (see Table 5.1). However, this conclusion might be affected by the statistical error in the time-averaged mean forces. If we use this barrier for the estimation of the reaction rate according to transition state theory[44-46] (see Appendix 5.A.1.4 for computational details), the predicted reaction rate of the two-channel model is k = 230.4 s^{-1} , which is faster than that obtained for the one-channel model (k = 15.7 s^{-1}). One should keep in mind that the two-channel model ends up with the final intermediate ^{3}(NDI1–[Ru^{II}–OO]$^{2+}$–NDI2) (S = 1) (see Scheme 5.1 and Figure 5.3) rather than an intermediate with a hydroperoxo ligand as in the one-channel model (^{2}([Ru^{III}–OOH]$^{2+}$–NDI) (S = 1/2))[17] as a result of the introduction of the second electron-transfer channel. Furthermore, the larger thermodynamic driving force ΔG^o = –10.9 kcal mol^{-1} (~0.47 eV) obtained in the two-channel model can be reasonably attributed to the accomplishment of the barrier-less fourth catalytic water splitting PCET step under the condition that the second dye NDI2 is photooxidized. This result suggests a relatively more stable final intermediate ^{3}(NDI1–[Ru^{II}–OO]$^{2+}$–NDI2) (S = 1) (see Scheme 5.1) lower in energy than an alternative in-between intermediate ^{3}(NDI1–[Ru^{III}–OOH]$^{2+}$–NDI2$^{+\bullet}$) (S = 1) (see Scheme A5.1).

In order to verify the feasibility of the entire proposed photocatalytic cycle for the two-channel model, the first half of the photocatalytic cycle was also investigated by using the same computational approach (see Appendix 5.A.6 for details). According to the results of our simulations, the first and second catalytic steps, starting from the initial intermediate ^{1}(NDI1–[Ru^{II}–OH$_2$]$^{2+}$–NDI2) (S = 0) and ending with the intermediate ^{3}(NDI1–[Ru^{IV}=O]$^{2+}$–NDI2) (S = 1) (see 1st & 2nd

PCET in Scheme 5.1), can proceed with a low activation free energy barrier of ~4 kcal mol^{-1} after the photooxidation of the two NDI dyes (see Figure A5.5). In this case we assume that one attacking water molecule is approaching H_{iii} while at the same time another attacking water molecule approaches H_{iv} (see Figure A5.4). The ^{1}(NDI1–[Ru^{II}–OH_2]$^{2+}$–NDI2) is in the S = 0 state due to the triplet molecular oxygen dissociating from the complex, leaving the singlet behind. The spins are parallel on the NDI in this first part (see Figure A5.4). and the spin is built up in steps. Apparently the Ru selects the appropriate spin from the NDI to build up its high spin magnetic ion state. Hence, the metal ion operates as a spin shuttle during catalysis. In the first part it selects the matching spin from the NDI to build up spin multiplicity, and in the second part it preserves the spin multiplicity and passes on a triplet to the oxygen.

5.3. Conclusions

In conclusion, the introduction of the second NDI dye in the dye–WOC–dye complex for photocatalytic water splitting provides an extra channel for ET, which enables the concurrent event of ET from the WOC to the two separate NDI dyes. The dynamical description of the proposed photocatalytic cycle of the two-channel model obtained with adiabatic AIMD simulations and explicit solvation demonstrates that the third and fourth catalytic steps can proceed one after the other without stable intermediates in between. Although the estimated activation free energy barrier of the combined third and fourth catalytic steps for the two-channel model is similar to that of the one-channel model, the introduction of the second ET channel removes one intermediate in the cycle: the system can now proceed without changing the total spin of the supramolecular complex, from the Ru=O intermediate to the final intermediate with a triplet molecular O_2 product. Overall, this study suggests that having the WOC coordinated to more than one dye at the photoanode of a DS-PEC device can have beneficial effects in the rate and efficiency of the photocatalytic cycle: this is achieved by having the co-photooxidation of the two dyes and an antiparallel spin alignment of the unpaired electrons on the dyes.

5.4. References

[1] Grätzel, M. *Nature* **2001,** *414*, 338-344.
[2] Berardi, S.; Drouet, S.; Francas, L.; Gimbert-Surinach, C.; Guttentag, M.; Richmond, C.; Stoll, T.; Llobet, A. *Chem. Soc. Rev.* **2014,** *43*, 7501-7519.
[3] Zhang, S.; Ye, H.; Hua, J.; Tian, H. *EnergyChem* **2019,** *1*, 100015.
[4] Yun, S.; Vlachopoulos, N.; Qurashi, A.; Ahmad, S.; Hagfeldt, A. *Chem. Soc. Rev.* **2019,** *48*, 3705-3722.
[5] Zahran, Z. N.; Tsubonouchi, Y.; Mohamed, E. A.; Yagi, M. *ChemSusChem* **2019,** *12*, 1775-1793.
[6] Xu, P.; McCool, N. S.; Mallouk, T. E. *Nano Today* **2017,** *14*, 42-58.
[7] Brennaman, M. K.; Dillon, R. J.; Alibabaei, L.; Gish, M. K.; Dares, C. J.; Ashford, D. L.; House, R. L.; Meyer, G. J.; Papanikolas, J. M.; Meyer, T. J. *J. Am. Chem. Soc.* **2016,** *138*, 13085-13102.
[8] Yu, Z.; Li, F.; Sun, L. *Energy Environ. Sci.* **2015,** *8*, 760-775.
[9] Ding, X.; Zhang, L.; Wang, Y.; Liu, A.; Gao, Y. *Coord. Chem. Rev.* **2018,** *357*, 130-143.
[10] Lyons, M. E. G.; Doyle, R. L.; Browne, M. P.; Godwin, I. J.; Rovetta, A. A. S. *Curr. Opin. Electrochem.* **2017,** *1*, 40-45.
[11] Xu, P.; Huang, T.; Huang, J.; Yan, Y.; Mallouk, T. E. *Proc. Natl. Acad. Sci.* **2018,** *115*, 6946-6951.
[12] Hammes-Schiffer, S. *Chem. Rev.* **2010,** *110*, 6937-6938.
[13] Gagliardi, C. J.; Vannucci, A. K.; Concepcion, J. J.; Chen, Z.; Meyer, T. J. *Energy Environ. Sci.* **2012,** *5*, 7704-7717.
[14] Hammes-Schiffer, S. *J. Am. Chem. Soc.* **2015,** *137*, 8860-8871.
[15] Horvath, S.; Fernandez, L. E.; Soudackov, A. V.; Hammes-Schiffer, S. *Proc. Natl. Acad. Sci.* **2012,** *109*, 15663-15668.
[16] Solis, B. H.; Hammes-Schiffer, S. *Inorg. Chem.***2014,** *53*, 6427-6443.
[17] Shao, Y.; de Ruiter, J. M.; de Groot, H. J. M.; Buda, F. *J. Phys. Chem. C* **2019,** *123*, 21403-21414.
[18] Swierk, J. R.; Mallouk, T. E. *Chem. Soc. Rev.* **2013,** *42*, 2357-2387.
[19] Wang, D.; Eberhart, M. S.; Sheridan, M. V.; Hu, K.; Sherman, B. D.; Nayak, A.; Wang, Y.; Marquard, S. L.; Dares, C. J.; Meyer, T. J. *Proc. Natl. Acad. Sci.* **2018,** *115*, 8523-8528.
[20] Maji, S.; Vigara, L.; Cottone, F.; Bozoglian, F.; Benet-Buchholz, J.; Llobet, A. *Angew. Chem. Int. Ed.* **2012,** *51*, 5967-5970.
[21] Garrido-Barros, P.; Funes-Ardoiz, I.; Drouet, S.; Benet-Buchholz, J.; Maseras, F.; Llobet, A. *J. Am. Chem. Soc.* **2015,** *137*, 6758-6761.
[22] Matheu, R.; Ertem, M. Z.; Benet-Buchholz, J.; Coronado, E.; Batista, V. S.; Sala, X.; Llobet, A. *J. Am. Chem. Soc.* **2015,** *137*, 10786-10795.
[23] Shao, Y.; de Groot, H. J. M.; Buda, F. *ChemSusChem* **2020**, *13*.
[24] Song, N.; Concepcion, J. J.; Binstead, R. A.; Rudd, J. A.; Vannucci, A. K.; Dares, C. J.; Coggins, M. K.; Meyer, T. J. *Proc. Natl. Acad. Sci.* **2015,** *112*, 4935-4940.
[25] Chen, Z.; Concepcion, J. J.; Hu, X.; Yang, W.; Hoertz, P. G.; Meyer, T. J. *Proc. Natl. Acad. Sci.* **2010,** *107*, 7225-7229.
[26] Shao, Y.; de Groot, H. J. M.; Buda, F. *J. Phys. Chem. Lett.* **2019**, *10*, 7690-7697.
[27] Kok, B.; Forbush, B.; Mcgloin, M. *Photochem. Photobiol.* **1970,** *11*, 457-475.
[28] Dau, H.; Haumann, M. *Biochim. Biophys. Acta, Bioenerg.* **2007,** *1767*, 472-483.
[29] Haumann, M.; Liebisch, P.; Müller, C.; Barra, M.; Grabolle, M.; Dau, H. *Science* **2005,** *310*, 1019-1021.
[30] Monti, A.; de Ruiter, J. M.; de Groot, H. J. M.; Buda, F. *J. Phys. Chem. C* **2016,** *120*, 23074-23082.

[31] Marx, D.; Hutter, J., *Ab initio molecular dynamics: basic theory and advanced methods*. Cambridge University Press, **2009**.
[32] Swart, M.; Ehlers, A. W.; Lammertsma, K. *Mol. Phys.* **2004,** *102*, 2467-2474.
[33] te Velde, G.; Bickelhaupt, F. M.; Baerends, E. J.; Fonseca Guerra, C.; van Gisbergen, S. J. A.; Snijders, J. G.; Ziegler, T., *J. Comput. Chem.* **2001,** *22*, 931-967.
[34] ADF2017, SCM, Theoretical Chemistry, Vrije Universiteit, Amsterdam, The Netherlands, http://www.scm.com.
[35] de Ruiter, J. M.; Buda, F. *Phys. Chem. Chem. Phys.* **2017**, *19*, 4208..
[36] CPMD, http://www.cpmd.org, Copyright IBM Corp., 1990–2019; Copyright MPI für Festkörperforschung Stuttgart, 1997–2001.
[37] Hartwigsen, C.; Goedecker, S.; Hutter, J., *Phys. Rev. B* **1998,** *58*, 3641-3662.
[38] Lin, I. C.; Coutinho-Neto, M. D.; Felsenheimer, C.; von Lilienfeld, O. A.; Tavernelli, I.; Rothlisberger, U., *Phys. Rev. B* **2007,** *75*, 205131.
[39] Ciccotti, G.; Ferrario, M., *Mol. Simul.* **2004,** *30*, 787-793.
[40] Agmon, N., *Chem. Phys. Lett.* **1995,** *244*, 456-462.
[41] de Grotthuss, C. J. T., *Biochim. Biophys. Acta, Bioenerg.* **2006,** *1757*, 871-875.
[42] Ensing, B.; Meijer, E. J.; Blöchl, P. E.; Baerends, E. J., *J. Phys. Chem. A* **2001,** *105*, 3300-3310.
[43] Costanzo, F.; Della Valle, R. G., *J. Phys. Chem. B* **2008,** *112*, 12783-12789.
[44] Eyring, H., *J. Chem. Phys.* **1935,** *3*, 107-115.
[45] Laidler, K. J.; King, M. C., *J. Phys. Chem.* **1983,** *87*, 2657-2664.
[46] Pollak, E.; Talkner, P., *Chaos* **2005,** *15*, 026116.

5.A. Appendix

5.A.1. Computational Details

5.A.1.1 Geometry Optimization at DFT Level

The OPBE exchange-correlation functional[1] and the TZP (triple-ζ polarized) Slater-type basis set[2] were employed in the geometry optimization of the initial state of the dye–WOC–dye complex. The OPBE functional has shown to be accurate in describing transition-metal complexes, including Ru-based WOCs.[3-6] In the geometry optimization, the continuous solvation model (COSMO[7-8]) for water was used. These calculations are performed with the ADF software package.[9-10]

5.A.1.2 Simulation Box

To obtain a realistic description of the catalytic reaction step, the solvent was explicitly introduced in the simulations. The solvent environment for the CPMD simulations was generated using Discovery Studio 2.5.[11] The solvent was equilibrated for 0.2 ns using the TIP3P model implemented in the CHARMM force field and CFF partial charge parameters at 300 K,[12] while the dye–$[WOC]^{2+}$–dye complex was kept fixed. The volume was then adjusted using constant pressure for 0.2 ns, after which the system was further allowed to evolve with constant volume for 2 ns. Periodic boundary conditions are applied with a time step of δt = 5 a.u. (1 a.u. = 0.0242 fs).

5.A.1.3 Free Energy Profile

To estimate the activation free energy barrier of the catalytic reaction step involving the O–O bond formation that is unlikely to occur spontaneously during the typical AIMD simulation time scale, constrained MD and the so-called Blue Moon approach were employed as a rare event simulation technique.[13-15] The reaction coordinate (in this case the distance between two oxygen atoms O_i and O_{ii}, $d(O_i \leftarrow O_{ii})$, as shown in Scheme 5.1) is constrained to a series of fixed values x in range of 2.5 – 1.6 Å after the initial equilibrium simulation and subsequent photooxidation of two NDI dyes along this reaction pathway. A time-averaged constraint force $\langle\lambda\rangle_x$ for each value of the reaction coordinate x is obtained, which should be equal to zero at an equilibrium or transition state. Based also on our previous work on a similar supramolecular complex, we can safely assume that

for a value of the reaction coordinate $d(O_i \leftarrow O_{ii})$ = 3.0 Å the system is in an equilibrium state with $\langle\lambda\rangle_{3.0\,Å}$ equals to zero.[16] The activation free energy barrier for this catalytic step is then established by interpolating the mean forces with a 100-point Akima splines function and integrating the signed forces $\langle\lambda\rangle_x$ along the reaction path.[17-20] Trajectory analysis and visualization for the CPMD output were carried out using VMD.[21-22]

5.A.1.4 Reaction Rate

The computed activation free energy barrier can be used to evaluate to what extent the geometry modification accelerates the rate of the third water oxidation step involving the O–O bond formation. According to transition state theory[23-25], the reaction rate (k) determined by the activation energy barrier (ΔG^*) can be expressed as

$$k = \frac{k_B T}{h} \cdot e^{-\frac{\Delta G^*}{RT}},$$

Where ΔG^* represents the activation free energy barrier, k_B, h, R and T are the Boltzmann constant, the Planck constant, the universal gas constant and thermodynamic temperature, respectively. One should keep in mind that in the DFT-based MD simulations protons are treated classically and thus proton tunneling effects are neglected. In the current calculation, only the activation energy barrier is considered as a main factor governing the reaction rate.

5.A.2. Expanded Reaction Pathways

Scheme A5.1. Expanded Reaction Pathways of the Two-Channel Model by a Ru-based dye–WOC–dye System[a]

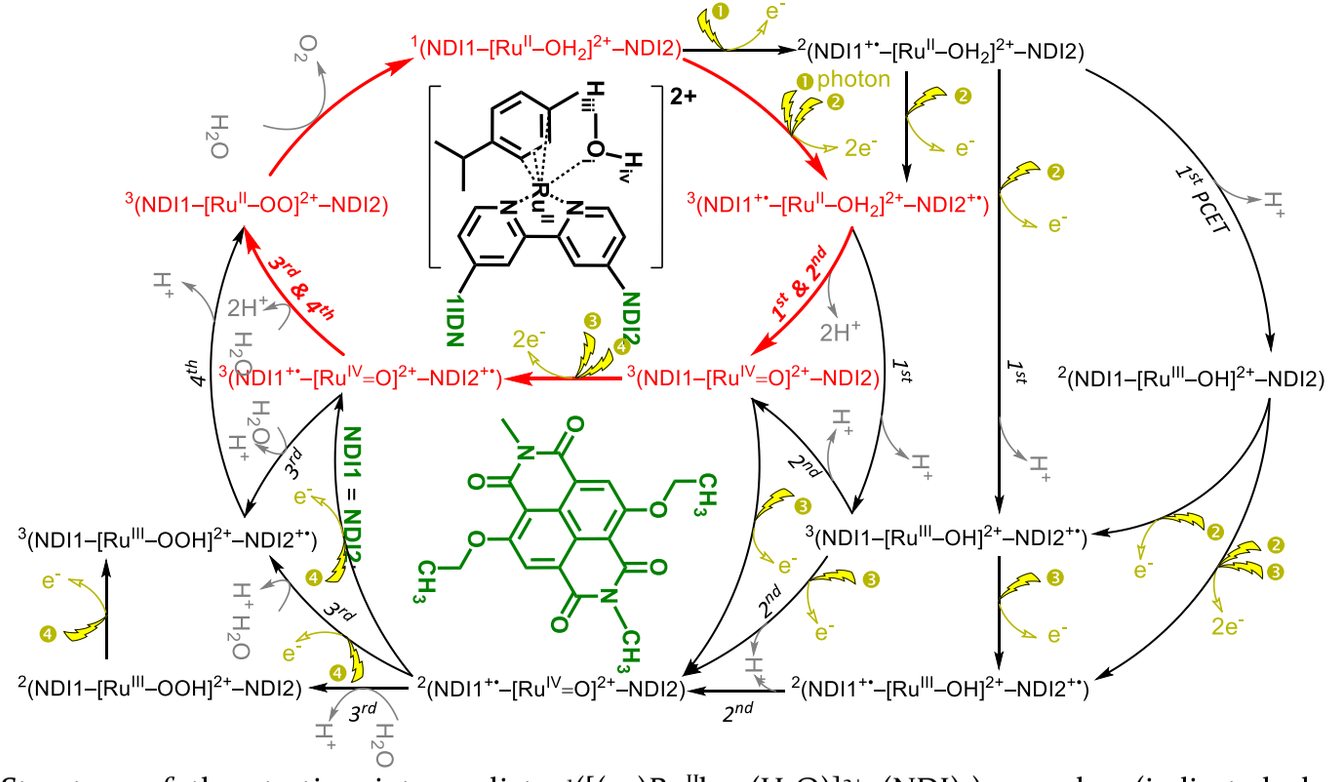

[a]Schematic Structure of the starting intermediate ^{1}([(cy)Ru^{II}bpy(H$_2$O)]$^{2+}$–(NDI)$_2$) complex (indicated shortly as ^{1}(NDI1–[Ru^{II}–OH$_2$]$^{2+}$–NDI2)) on the top of the scheme, as explicitly shown in the inset. It is assumed that each light flash induces an electron injection (golden arrows) from the NDI1/NDI2 to the semiconductor electrode or to the next stage in a tandem cell, leading to the photooxidation of NDI1/NDI2: NDI1/NDI2 → NDI1$^{+\bullet}$/NDI2$^{+\bullet}$. All the possible pathways for the dye–WOC–dye complex after introducing an extra NDI dye are considered in this scheme. In the current work we only focus on the case involving the cophotooxidation of two NDI dyes and the stable intermediates involved as shown in Scheme 5.1 are indicated in red. The transient states indicated in black are not investigated in this work.

5.A.3. Molecular Orbital and Electronic Structure

Table A5.1. Selected frontier molecular orbital energy levels and energy difference between the highest SOMO WOC and SOMO dye1/dye2 ($\Delta E_{SOMO\text{-}1}/\Delta E_{SOMO\text{-}2}$, in eV) of intermediate ^{3}(NDI1$^{+\bullet}$–[Ru^{IV}=O]$^{2+}$–NDI2$^{+\bullet}$) after the photooxidation of two NDI dyes.[a]

Intermediate	**^{3}(NDI1$^{+\bullet}$–[Ru^{IV}=O]$^{2+}$–NDI2$^{+\bullet}$)**	
	↓ ↑ ↑ ↑	
Energy level	**Orbital**	**Energy**
HOMO (*SOMO WOC*)	α	–6.302
HOMO–1 (*SOMO dye1*)	β	–6.482
HOMO–2 (*SOMO dye2*)	α	–6.509
HOMO–3	α	–6.773
HOMO–4	β	–6.806
HOMO–5 (*SOMO WOC*)	α	–6.838
$\Delta E_{SOMO\text{-}1}$		0.180
$\Delta E_{SOMO\text{-}2}$		0.207

[a]Only the unpaired electrons are indicated by vertical arrows explicitly (green for unpaired electron localized on the catalyst and blue for unpaired electron on the oxidized NDI$^{+\bullet}$). SOMO represents the singly occupied molecular orbital.

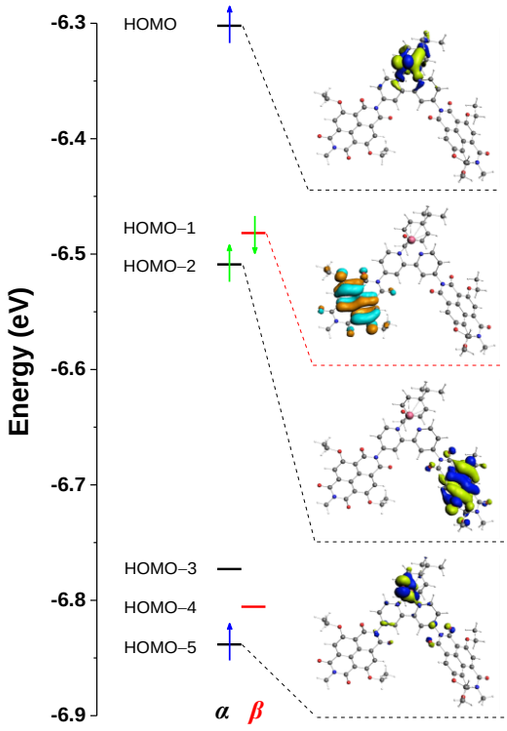

Figure A5.1. Selected frontier molecular orbitals of intermediate ^{3}(NDI1$^{+\bullet}$–[Ru^{IV}=O]$^{2+}$–NDI2$^{+\bullet}$) after the photooxidation of two NDI dyes computed with the ADF program using the OPBE functional and the TZP basis set. The left (black) and right (red) orbital energy levels refer to the α orbitals and β orbitals, respectively. Only the unpaired electrons are indicated by vertical arrows explicitly (blue for unpaired electron localized on the catalyst and green for the unpaired electron on the oxidized NDI$^{+\bullet}$). See **Table A5.1** for the molecular energy levels and the energy difference between SOMO WOC and SOMO dye.

5.A.4. Spin Density after Photooxidation of two NDI Dyes

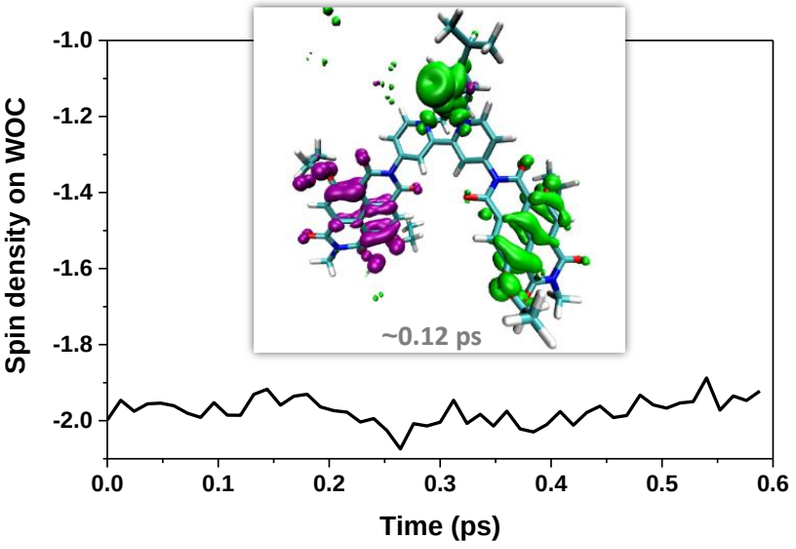

Figure A5.2. Spin density integrated over the part of the simulation box including the WOC along the free MD trajectory after the photooxidation of two NDI dyes. Inset shows the spin density isosurface computed at a snapshot taken at ~0.12 ps, clearly indicating two unpaired α electrons (↟ in green) localized on the catalyst, one unpaired β electron on NDI1 (↡ in purple), and one unpaired α electron on NDI2 (↟ in green). See Scheme 5.1 for the atomic labelling. The water molecules are omitted for clarity and only the intermediate ^{3}(NDI1$^{+\bullet}$–[Ru^{IV}=O]$^{2+}$–NDI2$^{+\bullet}$) is shown explicitly.

5.A.5. PT step during the Constrained 1.8 Å Simulation

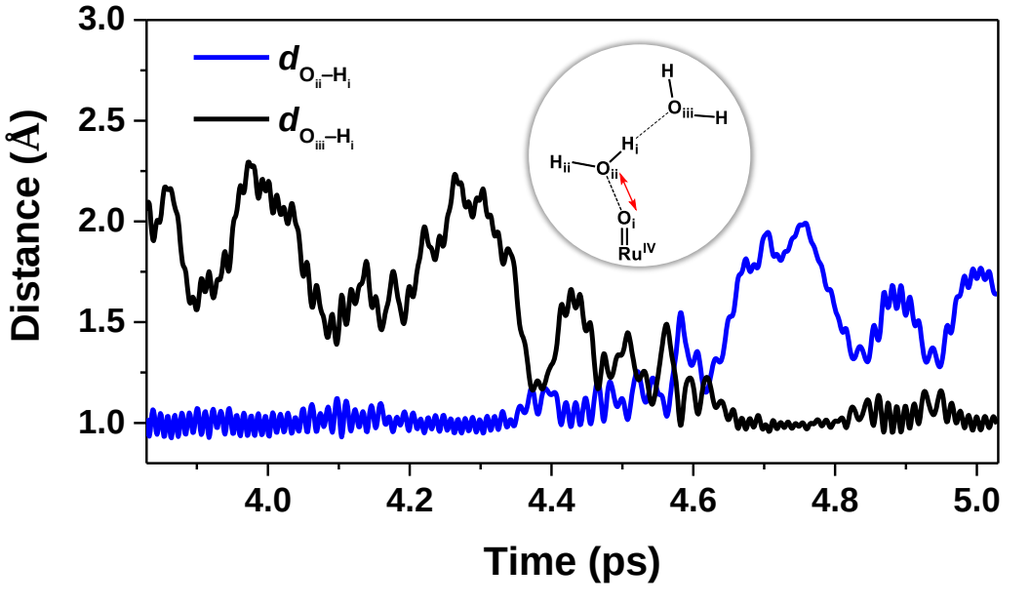

Figure A5.3. Time evolution of the geometrical parameters $d_{O_{ii}-H_i}$ (blue line) and $d_{O_{iii}-H_i}$ (black line) along the constrained MD trajectory with $d(O_i \leftarrow O_{ii})$ = 1.8 Å. The inset shows the schematic structure of the first two water molecules along the hydrogen-bonding network coordinated to the oxygen ligand. The time range is consistent with that in **Figure 5.1**.

5.A.6. First Half of the Catalytic Cycle

The initial geometry of the dye–WOC–dye complex ^{1}(NDI1–[Ru^{II}–OH$_2$]$^{2+}$–NDI2) (S = 0) was optimized at the DFT level employing the OPBE exchange-correlation functional[1] and the TZP (triple-ζ polarized) Slater-type basis set[2] with the ADF software package[9-10]. In the geometry optimization, the continuous solvation model (COSMO[7-8]) for water was used.

To obtain a realistic description of the catalytic reaction step, the solvent was explicitly introduced in the simulations. An orthorhombic box of dimensions 26.5 × 20.1 × 16.3 Å^3 with periodic boundary conditions containing the dye–WOC–dye solute ^{1}(NDI1–[Ru^{II}–OH$_2$]$^{2+}$–NDI2) (S = 0) together with 222 explicit water molecules was used in the AIMD simulations to get accurate predictions of the catalytic reaction, which was carried out with the CPMD program.[26]

Two reaction coordinates were considered in our constrained MD simulations, corresponding to the distances between H_{iii}/H_{iv} and the oxygen atom of its neighboring water molecule (see the atomic labeling in Scheme A5.1 and Figure A5.4). The reaction coordinates $d(H_{iii}\leftarrow O)$ as well as $d(H_{iv}\leftarrow O)$ are constrained to a series of fixed values x in range of 1.4 – 1.05 Å simultaneously after the initial equilibrium simulation and subsequent photooxidation of two NDI dyes. In this way, we assume that one attacking water molecule approaches to H_{iii} and another attacking water molecule to H_{iv} at the same time. The photooxidation of the NDI dyes (NDI1 and NDI2) was mimicked by removing two electrons from the simulation box after the initial equilibration simulation of the dye–WOC–dye system, after which a free MD (FMD) simulation of around 1.1 ps at room temperature was performed to equilibrate the oxidized state ^{3}(NDI1$^{+\bullet}$–[Ru^{II}–OH$_2$]$^{2+}$–NDI2$^{+\bullet}$) with the total spin S = 1.

According to the results of our simulations, one unpaired α electron (↟) is observed to localize on NDI1 and one unpaired α electron (↟) on NDI2 in the system (see inset (i) in Figure A5.4) when tracking the spin density along the free MD simulation after the photooxidation of the NDI dyes, which is in good agreement with the ground state of the oxidized complex ^{3}(NDI1$^{+\bullet}$–[Ru^{II}–OH$_2$]$^{2+}$–NDI2$^{+\bullet}$) (S = 1). The shortening of $d(H_{iii}\leftarrow O)$ and $d(H_{iv}\leftarrow O)$ from 1.4 Å to 1.1 Å induces the electron transfer from the WOC to the oxidized NDI dyes (see Figure A5.4a) The O_i–H_{iii} and O_i–H_{iv} bonds (see inset (iii) in Figure A5.4 for the atomic

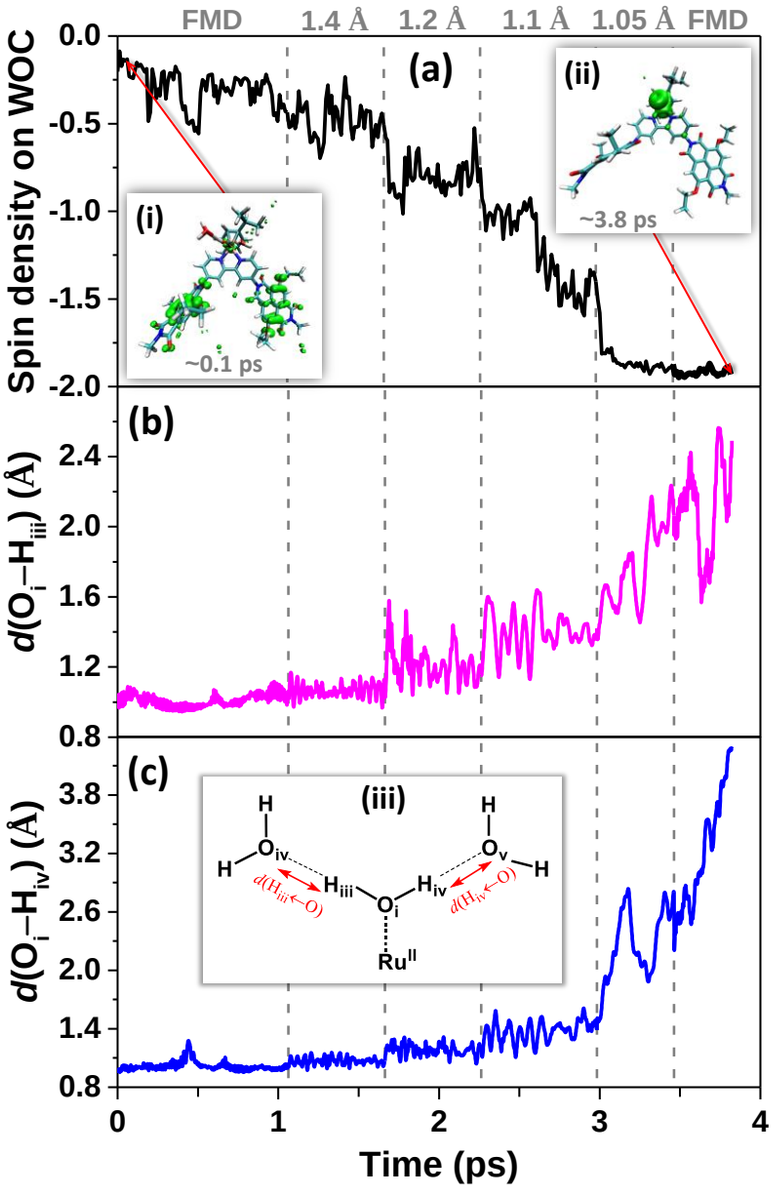

Figure A5.4. (a) Spin density integrated over the part of the simulation box including the WOC, time evolution of the geometrical parameters (b) $d(O_i–H_{iii})$ and (c) $d(O_i–H_{iv})$ along the free/constrained MD trajectories after the photooxidation of two NDI dyes. The inset (i) shows the spin density isosurface computed for a snapshot taken at ~0.1 ps, clearly indicating the intermediate $^3(NDI1^{+\bullet}–[Ru^{II}–OH_2]^{2+}–NDI2^{+\bullet})$ with one unpaired α electron (↟ in green) localized on each NDI dye. Inset (ii) shows the spin density isosurface computed for a snapshot taken at the end of the free MD (FMD) simulation, ~3.8 ps, clearly indicating the final intermediate $^3(NDI1–[Ru^{IV}=O]^{2+}–NDI2)$ with two unpaired α electrons (↟ in green) localized on the WOC. Inset (iii) shows the schematic structure of the first two water molecules along the hydrogen-bonding network coordinated to the ligand water molecule. For clarity, only the supramolecular complex and the attacking water molecules are shown explicitly. An integrated spin density value of –2 corresponds to two unpaired α electrons (↟). The value of the constrained reaction coordinate $d(H_{iii}←O)/d(H_{iv}←O)$ in the MD simulations is noted in grey.

labeling) finally break when we further shorten the $H_{iii}\cdots O_{iv}$ and $H_{iv}\cdots O_{v}$ distances to 1.05 Å (see Figure A5.4b and A5.4c), which occurs almost at the same time as the accomplishment of the electron transfer (see Figure A5.4a). No back-transfer of either an electron or a proton is observed after the release of the constraints from the system following the constrained 1.05 Å simulation. This confirms the stability of the final product ^{3}(NDI1–[Ru^{IV}=O]$^{2+}$–NDI2) (S = 1) with two unpaired α electrons localized on the WOC after the first and second catalytic PCET steps (see inset (ii) in Figure A5.4). All these results indicate that the first and second catalytic steps are able to proceed and complete at the same stage after the photooxidation of two NDI dyes.

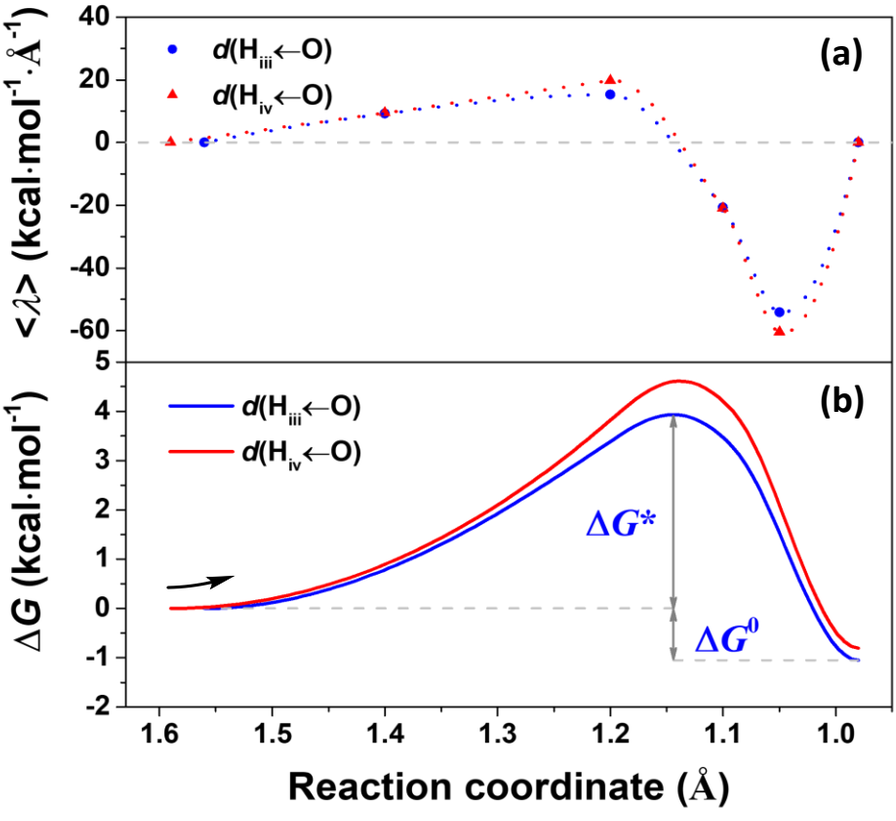

Figure A5.5. (a) Time-averaged constraint force represented by the Lagrangian multiplier <λ> computed for each constrained MD simulation as a function of the reaction coordinate $d(H_{iii}\leftarrow O)$ and $d(H_{iv}\leftarrow O)$ in the two-channel model. The mean force at the equilibrium distance $d(H_{iii}\leftarrow O)$ = 1.56 Å/$d(H_{iv}\leftarrow O)$ = 1.59 Å and $d(H_{iii}\leftarrow O)$ = 0.98 Å/$d(H_{iv}\leftarrow O)$ = 0.98 Å evaluated in the FMD simulations before and after the reaction, corresponding to the initial and final states along the reaction coordinates $d(H_{iii}\leftarrow O)$ and $d(H_{iv}\leftarrow O)$ respectively, have been assumed to be zero. The Akima splines (100 points) is used to interpolate the mean forces. (b) Free energy profile along the reaction coordinates $d(H_{iii}\leftarrow O)$ and $d(H_{iv}\leftarrow O)$ computed from thermodynamic integration.

Table A5.2. The calculated activation free energy barrier (ΔG^* in kcal mol^{-1}), reaction driving force (ΔG^o in kcal mol^{-1}), and the reaction rate (k in s^{-1}) corresponding to the reaction coordinates $d(H_{iii}\leftarrow O)$ and $d(H_{iv}\leftarrow O)$.

Reaction coordinate	ΔG^*	ΔG^o	k
$d(H_{iii}\leftarrow O)$	3.9	–1.1	8.9×10^9
$d(H_{iv}\leftarrow O)$	4.6	–0.8	2.8×10^9

Based on all the constrained MD simulations performed, the free energy profile along the reaction coordinates $d(H_{iii}\leftarrow O)$ and $d(H_{iv}\leftarrow O)$ of the oxidized complex $^3(NDI1^{+\bullet}–[Ru^{II}–OH_2]^{2+}–NDI2^{+\bullet})$ (S = 1) can be computed using the Bluemoon ensemble approach.[13-15] The time-averaged forces associated with the applied constraints $d(H_{iii}\leftarrow O)$ and $d(H_{iv}\leftarrow O)$, the interpolation of the time-averaged mean forces used for this analysis, and the corresponding free energy profiles obtained via thermodynamic integration of the oxidized complex $^3(NDI1^{+\bullet}–[Ru^{II}–OH_2]^{2+}–NDI2^{+\bullet})$ (S = 1) are presented in Figure A5.5. Table A5.2 summarizes the key thermodynamic parameters extracted from the free energy profiles corresponding to the reaction coordinates $d(H_{iii}\leftarrow O)$ and $d(H_{iv}\leftarrow O)$ for the first half of the catalytic water oxidation cycle.

The obtained free energy profiles for these two PCET processes reported in Figure S5 show similar activation free energy barriers $\Delta G^* \approx 3.9$ kcal mol^{-1} (0.17 eV) and $\Delta G^* \approx 4.6$ kcal mol^{-1} (0.20 eV), corresponding to the reaction coordinates $d(H_{iii}\leftarrow O)$ and $d(H_{iv}\leftarrow O)$ respectively in the two-channel model (see Table A5.2). This is consistent with the comparable activation barriers of the first and second catalytic PCET steps in the one-channel model[2, 16]. The maximum of the free energy profile corresponds to a reaction coordinate $d(H_{iii}\leftarrow O)/d(H_{iv}\leftarrow O)$ of 1.14/1.14 Å, suggesting an identified transition state with a smaller $H_{iii}\cdots O/H_{iv}\cdots O$ distance compared to that of the first/second catalytic PCET step in one-channel model. This concurrent event of the first two PCET processes is found to be fast and exothermic with the negative driving forces and high reaction rates $\Delta G^o \approx -1.1$ kcal mol^{-1} (0.05 eV)/$k \approx 8.9\times10^9$ s^{-1} and $\Delta G^o \approx -0.8$ kcal mol^{-1} (0.03 eV)/$k \approx 2.8\times10^9$ s^{-1} corresponding to the reaction coordinates $d(H_{iii}\leftarrow O)$ and $d(H_{iv}\leftarrow O)$, respectively, indicating that the selected NDI dyes are able to cooperatively drive this concurrent event in such a dye–WOC–dye system.

5.A.7. References

[26] Swart, M.; Ehlers, A. W.; Lammertsma, K. *Mol. Phys.* **2004**, *102*, 2467-2474.
[27] Monti, A.; de Ruiter, J. M.; de Groot, H. J. M.; Buda, F. *J. Phys. Chem. C* **2016**, *120*, 23074-23082.
[28] Carvalho, A. T. P.; Swart, M. *J. Chem. Inf. Model.* **2014**, *54*, 613-620.
[29] Groenhof, A. R.; Ehlers, A. W.; Lammertsma, K. *J. Am. Chem. Soc.* **2007**, *129*, 6204-6209.
[30] Conradie, J.; Ghosh, A. *J. Chem. Theory and Comput.* **2007**, *3*, 689-702.
[31] Vallés-Pardo, J. L.; Guijt, M. C.; Iannuzzi, M.; Joya, K. S.; de Groot, H. J. M.; Buda, F. *ChemPhysChem* **2012**, *13*, 140-146.
[32] Klamt, A. *J. Phys. Chem.* **1995**, *99*, 2224-2235.
[33] Klamt, A.; Jonas, V. *J. Chem. Phys.* **1996**, *105*, 9972-9981.
[34] te Velde, G.; Bickelhaupt, F. M.; Baerends, E. J.; Fonseca Guerra, C.; van Gisbergen, S. J. A.; Snijders, J. G.; Ziegler, T. *J. Comput. Chem.* **2001**, *22*, 931-967.
[35] ADF2017, SCM, Theoretical Chemistry, Vrije Universiteit, Amsterdam, The Netherlands, http://www.scm.com.
[36] Accelrys Software Inc. Discovery Studio Modeling Environment, Accelrys Software Inc.: San Diego, 2012.
[37] Brooks, B. R.; Bruccoleri, R. E.; Olafson, B. D.; States, D. J.; Swaminathan, S.; Karplus, M. *J. Comput. Chem.* **1983**, *4*, 187-217.
[38] Ciccotti, G.; Ferrario, M. *Mol. Simul.* **2004**, *30*, 787-793.
[39] Ensing, B.; Meijer, E. J.; Blöchl, P. E.; Baerends, E. J. *J. Phys. Chem. A* **2001**, *105*, 3300-3310.
[40] Costanzo, F.; Della Valle, R. G. *J. Phys. Chem. B* **2008**, *112*, 12783-12789.
[41] Shao, Y.; de Ruiter, J. M.; de Groot, H. J. M.; Buda, F. *J. Phys. Chem. C* **2019**, *123*, 21403-21414.
[42] Otter, W. K. d.; Briels, W. J. *J. Chem. Phys.* **1998**, *109*, 4139-4146.
[43] Sprik, M.; Ciccotti, G. *J. Chem. Phys.* **1998**, *109*, 7737-7744.
[44] Bernasconi, L.; Baerends, E. J.; Sprik, M. *J. Phys. Chem. B* **2006**, *110*, 11444-11453.
[45] Bernasconi, L.; Kazaryan, A.; Belanzoni, P.; Baerends, E. J. *ACS Catal.* **2017**, *7*, 4018-4025.
[46] Humphrey, W.; Dalke, A.; Schulten, K. *J. Mol. Graphics* **1996**, *14*, 33-38.
[47] VMD - Visual Molecular Dynamics. *Theoretical Chemistry and Computational Biophysics Group*, University Of Illinois: Urbana, 2016.
[48] Eyring, H. *J. Chem. Phys.* **1935**, *3*, 107-115.
[49] Laidler, K. J.; King, M. C. *J. Phys. Chem.* **1983**, *87*, 2657-2664.
[50] Pollak, E.; Talkner, P. *Chaos* **2005**, *15*, 026116.
[51] CPMD, http://www.cpmd.org, Copyright IBM Corp., 1990–2019; Copyright MPI für Festkörperforschung Stuttgart, 1997–2001.